DOI: 10.1002/((please add manuscript number))

Article type: Full Length Article

Aging of Au(111) at ambient conditions: understanding the surface dynamics of adventitious carbon contamination and gold work function changes

Nicholas Turetta,[1,2] Francesco Sedona,[2] Andrea Liscio,[3] Mauro Sambi,[2*] Paolo Samorì[1*]

[1] Université de Strasbourg, CNRS, ISIS UMR 7006, 8 allée Gaspard Monge, F-67000 Strasbourg, France. Email : samori@unistra.fr

[2] Dipartimento di Scienze Chimiche, Università degli Studi di Padova, Via Marzolo 1, 35131 Padova, Italy. Email : mauro.sambi@unipd.it

[3] Istituto per la microelettronica e microsistemi (IMM), Unità di Roma, Consiglio Nazionale delle Ricerche (CNR), Via del Fosso del Cavaliere 100, 00133 Roma, Italy.

Keywords: Gold, work function, adventitious carbon contamination, Kelvin probe, photoemission yield

Abstract (max 200 words for ASS)

Gold is an inert noble metal displaying superior chemical stability that renders it a suitable component for the manufacturing of electrodes for various types of devices. Despite being widely employed, the variation of gold surface properties occurring upon the material's aging at ambient conditions have been often disregarded. While it is well-known that the contamination of a metallic surface can have a dramatic impact on its properties, the process of contamination itself is poorly understood. Changes of the work function by fractions of an electron-volt are commonly observed in gold surfaces that are processed at ambient laboratory conditions, but an exhaustive comprehension and control of this phenomenon is still lacking. We present here a multiscale characterization of Au(111) surfaces aimed to unravel the surface dynamics underlying the air contamination. The visualization of the adventitious carbon contamination via atomic force microscopy is key to rationalize the mechanisms of surface reorganization that govern the observed variations of the work function.

Introduction

Gold is classified as a noble metal by virtue of its resistance to corrosion and oxidation. Clean gold is characterized by a hydrophilic and high-energy surface, but, despite its inertness, the clean surface gets contaminated with small organic molecules within a few minutes of exposure to ambient air.[1] In fact, the so-called adventitious carbon (AC)[2,3] is ubiquitously present on the surface of inorganic materials, such as metals,[4–7] silicon dioxide,[8–11] or indium tin oxide (ITO).[12–14] This airborne contamination is known to form a layer that changes the wettability of these surfaces rendering them hydrophobic upon air exposure.[1,15–17] Gold is widely employed both in applied and fundamental research (e.g. opto-electronic device fabrication, adsorption studies, electrochemical detection) and it is also a suitable material for gravitational waves detection (Gravity Probe B,[18] UV-LED,[19] and LISA Pathfinder[20]). The control of adventitious contamination is of critical importance for the above-cited applications, as surface cleanliness and uniformity are among the key requirements to obtain reliable and reproducible results.[21–23] For example. in ultra-high vacuum (UHV) environments, sputter-cleaning via ion-gun bombardment followed by thermal annealing is used to remove organic contaminants to yield clean metallic surfaces.[24–28] Alternatively, thin films of pure gold can also be produced in-situ via thermal evaporation,[17] sputtering deposition[29,30] or e-beam evaporation.[29] If gold surfaces are processed at ambient pressure (e.g. used as a substrate for the deposition of thin film or for the adsorption of biomolecules, monolayer films or nanoparticles) cleaning and/or pre-treatment protocols are often necessary, even for freshly evaporated metals.[31] Interestingly, Zimmerling and Batlogg reported that the magnitude of the contact resistance of a metal-semiconductor junction can be reduced by exposure of the metal interface to air before the semiconductor deposition,[32] but, in general, a cleaning protocol is implemented depending on the target application. In general, the choice of the cleaning procedure depends on the target application. Different combinations of dry treatments (e.g. flame annealing[33], plasma cleaning,[34–36] ultraviolet/ozone (UV/O_3),[37–39] mechanical polishing[40]) and wet treatments (e.g. rinsing and/or ultrasonication in a cleaning solvent, (electro)chemical treatments[40–43]) are commonly employed during the early stages of sample preparation prior to further processing. Residual contamination or structural changes induced by the treatment might influence, for instance, the electrochemical response of gold, still without completely preventing its functionality.[42] In other cases, instead, as in surface force or molecular adsorption studies done via SPM,[21] a very smooth and clean surface is required. The AC contamination usually represents the uppermost layer and its presence heavily affects the measurement of surface-sensitive physical properties; for example, Gomez-Herrero et al.[44] showed via Kelvin probe force microscopy (KPFM) that carbon contamination can locally change the work function (WF) of a highly-oriented pyrolytic graphite (HOPG) sample (freshly cleaved in ambient air and transferred inside a vacuum chamber at

the pressure of 1×10^{-5} mbar) by ≈ 0.2 eV. Ideally, the complete removal of AC is required for the correct determination of the WF by means of ultraviolet photoelectron spectroscopy (UPS), especially when relatively small WF variations are expected (e.g. differences arising from crystallographic orientations of Au[28] and Ag[27] single crystals). However, the removal of the AC layer often implies the transfer of the sample in a UHV environment and the invasive cleaning (e.g. via sputtering) which can determine a major modification of the surface structure. Hence, with the aim to characterize the system in conditions as similar as possible to those of working devices, macroscopic Kelvin probe (KP) and photoelectron yield spectroscopy (PYS) are widely employed to estimate the WF or the ionization potential (IP) of materials in ambient atmosphere.[45–47] In addition, in order to preserve the integrity of the sample, surface analyses can be performed without removing the AC layer and correction models are employed for data analysis, as in X-ray photoelectron spectroscopy (XPS)[3,8,48–50] and X-ray reflectometry (XRR).[11,51,52] While many efforts have been dedicated to the removal of the AC layer, the process of contamination itself is still poorly understood. The evolution of the surface properties of a metallic sample during ambient exposure is overlooked as well, despite large changes are observed depending on the preparation conditions and the environmental history of the sample[53,54]. Each storage, processing or cleaning step might also affect the surface properties such as work function,[38,55] wettability,[21,36] surface composition.[24,38,56] During the experimental practice, the identification of the source(s) of contamination is highly sought after. Since the formation of the AC layer is a direct consequence of the exposure of the sample to a complex medium, i.e. ambient air, a plethora of different volatile species are interacting with the surface. An analytical and rational approach studying the adsorption and desorption of specific compounds[57,58] fails to comprehensively describe the actual dynamics of surface contamination. Instead, a more accurate description of the system could be achieved if the structure and morphology of the contamination layer could be determined experimentally. Scanning probe microscopy (SPM) techniques, such as atomic force microscopy (AFM), scanning tunneling microscopy (STM) and KPFM, can provide direct insight into local changes of the surface properties. In principle, the presence of an AC superficial layer could be detected with these techniques and its properties mapped as two-dimensional grids of data points. However, many complications are associated with the characterization of contamination in general. For instance, if the contamination layer has a uniform thickness, chemical composition and spatial distribution, only limited information can be extracted from surface imaging even at the best operating conditions of the instrument, thereby rendering the contamination undistinguishable from the substrate. In addition, the distinction between features arising from surface contamination and features peculiar to the clean surface is further hindered in samples characterized by a corrugated surface (e.g. polycrystalline Au with randomly oriented crystallites). Conversely, the surface of

Au(111) on mica can exhibit atomically flat terraces which can serve as ideal platforms to study the dynamics of AC contamination.

In this work, we present the dynamics of surface contamination of Au(111) grown on mica substrates upon exposure to ambient air. The evolution with time of the experimental work function during the contamination process was compared with the trend of the other surface properties. Two separate regimes were identified and rationalized by means of surface characterization techniques. The growth of the AC contamination layer, due to the continuous accumulation of airborne contaminant species, were monitored via AFM, revealing their tendency to form nanometric aggregates which diffuse and merge, thereby affecting the properties of the Au surface at different length scales. In particular, we found that the AC contamination determines large variabilities in the WF of the Au samples (e.g. for polycrystalline Au the WF is found to range between 4.4 and 5.4 eV).[53] Towards this end, we finally showed that the WF of Au(111) can be reversibly changed by a few tenths of eV by storing the sample in an open air container or in a sealed container placed in the same room.

Results and discussion:

Kelvin Probe (KP) and photoemission yield spectroscopy (PYS) measurements

The macroscopic work function (WF) and contact potential difference (CPD) changes occurring upon aging of Au(111) samples during exposure to ambient conditions were assessed via PYS[59] and KP, respectively. We recorded the WF and CPD vs time curves of template-stripped (TS) Au(111) samples, shown in Figure 1a. Mica TS Au(111) thin films are often used as clean hydrophilic surface,[1,21] thus its characterization is interesting both from a fundamental and an applicative perspective. The measured WF and CPD show a similar trend: i) a fast decrease in the first 15 minutes, ii) reaching the minimum after about 60 minutes, and iii) a subsequent slow and partial recovery of the initial values due to an equilibration process which involves the gold surface and its contamination layer. Remarkably, the WF (CPD) of Au(111) was found to change in a range of 0.5 eV within the first two hours of exposure to ambient conditions, in a range of values comparable to those detected by Wan et al. via UPS analysis.[5] The fast WF decrease variation started from values slightly below those of sputter cleaned (SC) Au(111), determined to be 5.30 ± 0.05 eV in UHV.[28] A similar change in WF was also observed by Kinoshita et al.[60] as a function of the adventitious carbon (AC) coverage of Au samples in UHV. The CPD was then monitored on a longer timescales via KP and PYS on the very same sample, as shown in Figure 1b. The slow overall increase of the CPD (i.e. few tens of mV per day) indicates that the equilibration process of the gold surface with the environment requires days or weeks to be completed. After one month of continuous exposure to the ambient atmosphere, no significant CPD increase was recorded. The reliability of such measurement, also in terms of long-term stability of the tip WF (WF_{tip}), was guaranteed by two reference samples: a freshly exfoliated HOPG sample and a Au(111) on mica sample that was stored inside the open air KP setup, in close proximity to the tip (calibration data are reported in Figure S1a).

To rationalize the physics underlying the observation of two distinct regimes of WF variation, a comprehensive understanding of the AC layer formation and surface dynamics is required. A first evidence of the AC layer formation is given by the time evolution of the slope of the photoelectron yield (PY) Fowler plots (examples reported in Figure S1b), which is known to be correlated to the thickness of the contamination layer.[61,62] By monitoring the relative decrease of the PY slope (%S) it is possible to obtain an indirect proof of the build-up of the AC layer, as shown in Figure 1c. A second evidence is provided by the change in the surface wettability, induced by the formation of the contaminant layer, as evidenced by the water contact angle (CA) increase over time. Noteworthy, a similar increase in the water CA vs time curve was previously reported by Chai and Klein[21]. The CA and %S curves in Figure 1c, decaying at a similar rate, assume an almost constant value within two

hours, suggesting that the increased hydrophobicity of the gold surface is correlated to the adsorption of airborne contaminant species. These experimental observations indicate that the dominant mechanism governing the change of the WF during the first hour of aging is the formation of a contamination layer. This WF change can be described in terms of the "pillow effect": the presence of adsorbates on the metal surface leads to a compression of the surface electronic dipole, thus lowering the WF.[53] While the rapid initial decrease in CPD is limited to the first 15 minutes, the bump in the CPD curve (obtained between 15 and 45 minutes) might indicate the temporal boundary between the rapid formation of a kinetic monolayer of contamination and its subsequent structural rearrangement into a more stable layer.

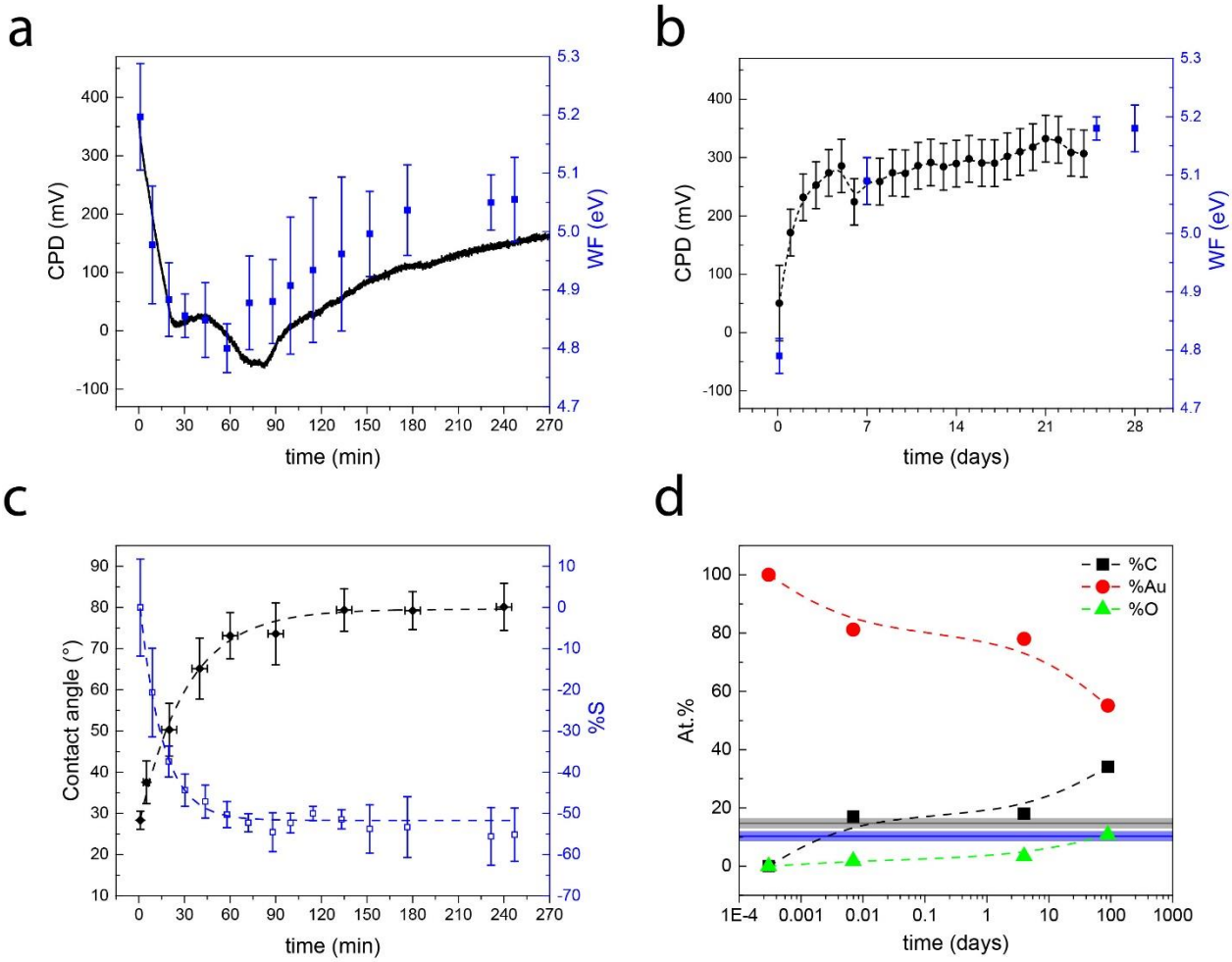

Figure 1: Surface properties (WF, CA, AC layer, atomic composition) of clean Au(111) as a result of the exposure to laboratory environment for different time periods. (a) Short and (b) long term WF and CPD measurements. (a) example of CPD (black solid) curve, determined by KP, versus average WF data (blue squares), determined by PYS, collected from TS Au(111) thin films at ambient conditions. The reported photoelectric WF values were estimated from the onset of photoelectron yield (PY) Fowler plots. The tip calibration for CPD measurements is WF_{tip} = 4.83 eV. (b) Long term acquisition of CPD data (black circles) vs. PYS WF data (blue squares) from the same Au(111) on mica sample during exposure to ambient air. (c) AC layer formation: contact angle (black squares) vs. relative decrease of PY slope (%S, blue empty squares). (d) Au surface composition: Atomic

percentage of the most abundant elements on an air-contaminated gold surface (Au, C and O) extrapolated from XPS analysis as a function of time (semi-logarithmic scale). The surface composition of the sample cleaned in UHV is assigned to a finite time value for convenience. Compositional data was then collected after 10 minutes, 4 days and 3 months of aging at ambient conditions. The blue horizontal dashed line and the light blue area represent the average and standard deviation of the %C value of a 0.7 PPP monolayer on Au(111), 11 ± 2%, while the grey solid line and area represent the same value after correction for a complete PPP monolayer, 16 ± 2% (see Section S1).

In order to determine the surface atomic composition of Au(111) upon aging at ambient conditions it was necessary to quantify the amount of carbon contaminant species accumulating and to further investigate the timescales of formation of the AC layer. The accumulation of C and O of sputter-cleaned (SC) Au(111) on mica samples was explored by means of XPS for different aging times, after 10 minutes, 3 days and 3 months of aging at ambient conditions, as shown in Figure 1d. These samples were cleaned under UHV conditions via repeated cycles of Ar^+ sputtering and thermal annealing (details in the Experimental Section). The sputtering and annealing cycles on sputter-cleaned (SC) Au samples were stopped when no contaminant species were detected by UHV-STM imaging and XPS (see Figure S2). The compositional data, reported on a logarithmic time scale, show that a rapid decrease in the Au fraction occurs within the first ten minutes, as the sum of C and O fractions is around 20%, confirming that organic contaminant species readily adsorb on the surface.

A fast contamination process is somehow expected if we compare %C after 10 minutes at ambient conditions ($\%C_{10min}$ = 18%) with that obtained from an Au(111) surface decorated with a (partial) monolayer of poly(*p*-phenylene) (PPP) wires ($\%C_{PPP}$ = 11%) starting from 4,4″-dibromo-*p*-terphenyl. (DBTP).[22] This molecular system was chosen as a reference to estimate the signal from a monolayer of known carbon-based contaminant (further details are provided in Section S2). The %C of the airborne contaminant layer after 10 minutes is comparable to the %C obtained from an ideal, fully covering, close-packed self-assembled structure of PPP on Au(111) (chemical composition data and C 1s spectra reported in Figures 1d and S1b, respectively). The immediate adsorption of carbon contaminants on sputter-cleaned surfaces was similarly observed in polycrystalline silver samples.[24] SC samples exposed for 10 minutes to ambient air remained for at least three hours at pressures above 10^{-6} mbar (the time for transfer to ambient air plus the time required to pump down the fast entry chamber), thus having supplementary time to build up the contamination layer.

The relatively small decrease of %Au that was observed after 3 days of aging (%Au ≈ 75%) suggests that the accumulation of additional contaminant species on the surface occurs more slowly. After the fast kinetics of formation of the first overlayer, the subsequent growth of the AC layer occurs at a

much slower rate. The Au fraction calculated after 3 months of aging is further decreased to about 60%, confirming that the contamination process at ambient conditions does not stop within a few days. After this longer period, the oxygen fraction increases above 10%, suggesting the presence of adsorbed water and/or oxidized species on the surface as a direct consequence of the action of environmental water and oxygen.[3] Altogether, XPS, CA and %S measurements provided unambiguous evidence that the formation of a contamination layer occurs within tens of minutes after exposure to ambient conditions. The rapid initial drop of the WF can be explained by means of these techniques, however, none of them is able to elucidate why the WF starts to increase after the first few hours of aging. In other words, the second part of the curve needs a more accurate description of the AC layer in order to be explained.

Dynamics of surface contamination of Au(111) at ambient conditions

The topography of Au(111) on mica samples is characterized by atomically flat terraces that are suitable to study the dynamics of formation of the AC contamination. The AFM images reported in Figures 2a and 2b were recorded in non-contact mode and illustrate the effect of the aging on Au(111) after 3 hours and 3 days from the transfer to ambient air, respectively. The monitoring of the surface contamination upon exposure to ambient air was done on SC Au(111) films supported on mica substrates. In the inset of Figure 2a, many terraces with steps in height *h* of 1–2 Å can be observed on the Au(111) surface (with the z-noise on atomically flat regions of the Au(111) terraces being around 0.4 Å). These topographic features can be ascribed to the presence of contaminant aggregates.

The height and size of these aggregates increases with time, as observed upon monitoring the surface after three days (Figure 2b). In some cases, the height of the aggregates exceeded 1 nm (range 0.5–1.9 nm). These aggregates can be either found close to a terrace edge or at an inner region of the terrace and their relative position within a terrace can affect their mobility. The migration dynamics of contaminant aggregates is better visualized through the movie available in the Supporting Information (Supporting Video 1). Such movie shows that aggregates can migrate within the terrace and two nearby aggregates can merge. Aggregates at a terrace edge tend to remain at their position, while aggregates at inner regions of the terraces may exhibit displacements of few tens of nanometers in successively recorded images (each frame corresponds to approximately 45 minutes in real time). The occurrence of these events reveals the dynamic nature of contaminants adsorbed onto Au(111) surfaces. In order to provide further demonstration that the contamination of Au(111) surfaces mediated by airborne contaminant species may occur ubiquitously, we compared the AFM topography of samples that were independently aged in two different laboratories (the first one placed in Padova and the second one in Strasbourg, see Figure S5x) for three weeks at ambient conditions.

In both cases, Au(111) on mica samples “as received” from the manufacturer were imaged before and after the aging period, without prior cleaning. Despite the possible differences in surface composition, arising from the presence of diverse contaminant species in the ambient air of the two laboratories, a similar growth of airborne contaminant aggregates in both laboratories is confirmed by the AFM topography images.

However, by using “as received” samples, no information about the first minutes of contamination after the ambient exposure is known. Likewise, by using SC Au, it is possible to investigate the contamination dynamics at a timescale shorter than the time required for the venting procedures of the vacuum chamber and the transfer to the AFM stage (that typically lasts ca. 2 hours). During this time period, the SC samples suffer from the exposure to the contaminant species entering in the vacuum chamber. Therefore, to circumvent such problems, we employed template-stripped (TS) Au(111) to study the contamination processes as soon as the “clean” surface was exposed to ambient air.

The nucleation of contaminant aggregates starts to occur since the first minutes of air exposure as it can be seen in Figures 2c-f, with black arrows marking round-shaped objects with a positive phase shift and heights similar to those in the inset of Figure 2a which are already found at t = 30 min. A different phase response is recorded when the tip scans an aggregate as shown in Figure S4. Under our experimental conditions (intermittent contact mode in the attractive regime), a positive phase shift is expected for an increasing sample viscosity and a decreasing elastic modulus[63] in agreement with the aggregates being amorphous clusters of organic species.

As evidenced in Supporting Video 2, during the first hours of aging of the TS Au sample, we also observed the modification of the surface, arising from the contamination process and/or the relaxation of the mechanical stress induced by the peel-off procedure. Indeed, the comparison of the topography image after 30 minutes, Figure 2c, and after 3 hours, Figure 2e, shows that the smallest Au ad-islands and the step edges with the smallest curvature radius disappearing because included in the surface (part 3 of Supporting Video 2). Moreover the phase image reported in Figure 2d is characterized by bright positive-shifted curved lines that can be attributed to the step edges (red dashed line in Figure 2d) but also by the presence of some unexpected straight lines aligned along the three [110] directions of Au(111) (black dashed lines in Figure 2d) that are barely visible in the topography images. The nature of these straight lines seems to be related to linear lattice defects indeed, as evidenced in the part 3 of the Supporting Video 2, these linear features move and reorganize until, after 3 hours, they almost disappear as evident in Figure 2f. To the best of our knowledge there is only one previous example which demonstrates that defective regions can induce a change in the surface mechanical

properties that can be resolved by phase imaging.[64] Therefore, the freshly TS Au shows a low level of AFM-visible contaminant aggregates but a large number of structural defects.

The above-discussed AFM images well summarize the surface processes occurring during aging and help us to describe the AC layer as a dynamic system consisting of an overlayer of contaminant species that can accumulate into mobile contaminant aggregates. Interestingly, the surface modification is occurring at around the same aging time of the CPD bump and CPD curve minimum, thereby suggesting that the structural rearrangement of the gold surface and its AC layer may also have an impact on the observed WF on the hour timescale.

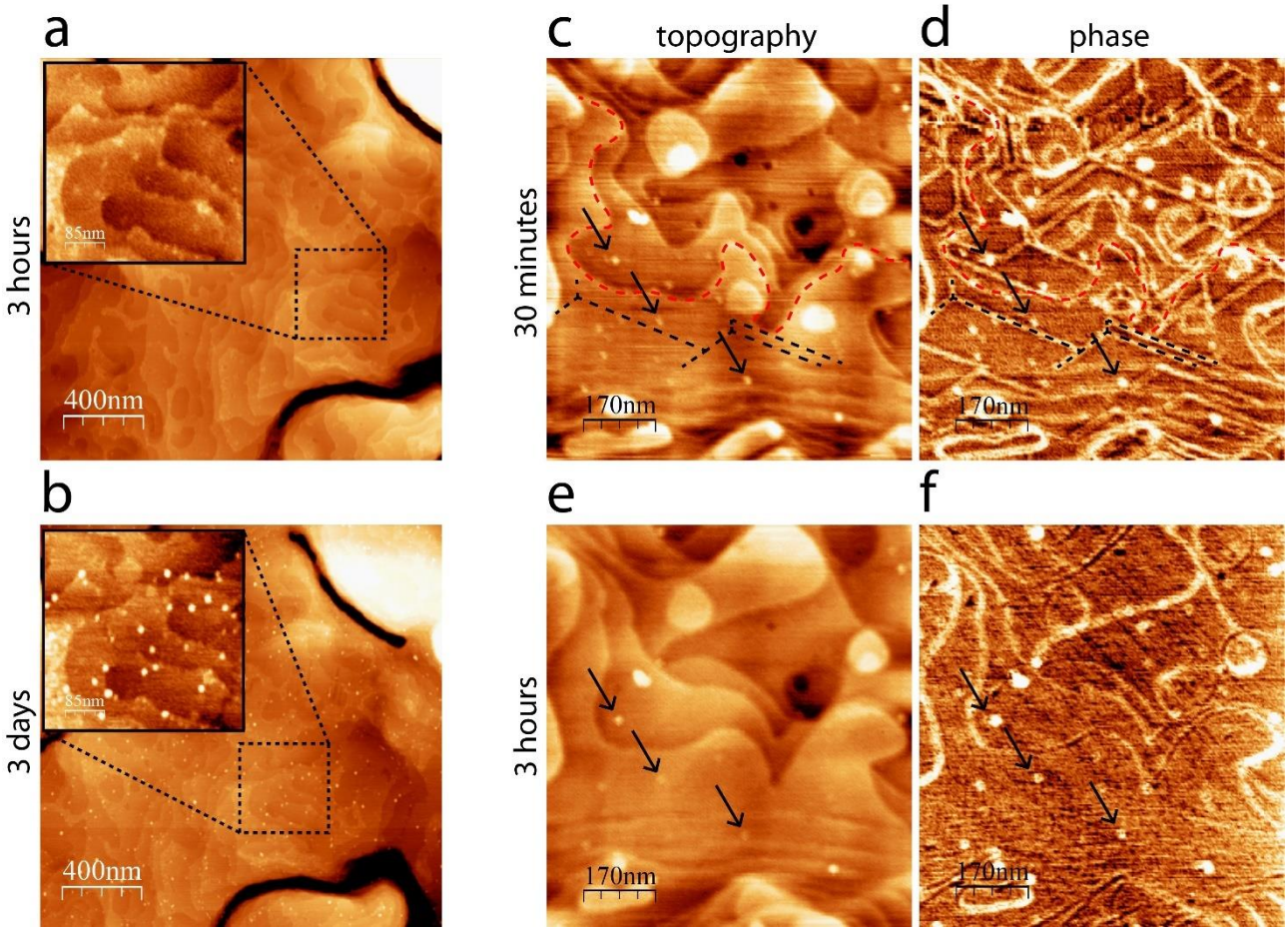

Figure 2: Ambient-AFM topography images of a SC Au(111) on mica surface collected in non-contact mode after (a) 3 hours and (b) 3 days of aging at ambient conditions. A magnification of the same dashed area is provided in the inset of the images. Ambient-AFM (c, e) topography and (d, f) phase contrast images of a TS Au(111) surface collected in intermittent contact mode (c, d) at t = 30 min and (e, f) t = 3 hours from peeling-off. Contaminant aggregates are indicated by black arrows. An example of terrace edge profile is indicated by a red dashed curved line, while the three principal [110] directions are indicated by black dashed straight segments. The Z-scale is: (a) 4.3 nm, (b) 5.1 nm, (c) 1.8 nm, (d) 2°, (e) 2.0 nm, (f) 2°. The number density of aggregates in (b) is n_S: 350 μm^{-2}. The entire sequence of the images is provided in Supporting Videos 1 and 2.

Lateral size correction of contaminant aggregates imaged via AFM

In order to quantify the real width of the features imaged by AFM it is necessary to take into account the lateral broadening effect due to the finite size of the tip. Moreover, more pronounced effects may arise from tip degradation due to the long imaging times, yet the use of a non-contact imaging mode helps to preserve the integrity of the tip. Contaminant aggregates grew in lateral size (d) and height (h) during the aging period and the increase in their apparent lateral size (d_{app}) is not simply related to tip deterioration. In general, if the experimental AFM topography is affected by the tip convolution artifact, only apparent values for lateral size (d_{app}) and height (h_{app}) can be measured. To quantify the effective d of the aggregates, a simple geometrical correction model has been employed in order to remove the profile broadening (Δ) due to the finite size of the tip[65,66]. The mathematical derivation of the correction model is summarized in Section S4.

For the sake of example, we applied the correction model to two aggregates: one imaged via non-contact mode (Figure 3a) and one imaged via intermittent contact mode (Figure 3b). Contaminant aggregates on gold can be described by a spherical cap of height h and lateral size d (see Figure 3e). The lateral size d after correction evaluates to 18 ± 3 nm and 25 ± 3 nm, for the cyan and blue profiles reported in Figures 3c. The two examples considered, differing in the AFM imaging mode and probe type, show aggregates which are significantly unalike in lateral size after correction. Note here that the geometry of the aggregates is much “more flat” than it appears in the profiles. In the cartoon of Figure 3d, we propose a simplified picture of the microscopic geometry that characterizes the airborne contamination of Au(111) surfaces, where the “real” size aggregate is indicated with a dashed profile. The geometrical parameters listed in Table 1 (referred to the reported AFM images) show a clear increasing trend of d with increasing h. More details about the differences between non-contact and intermittent-contact imaging modes are provided in Section S4. As a reference to the reader, the range of geometrical parameters characteristic of the aggregates in each Figure is reported in Table 2.

Figure	h (nm)	d_{app} (nm)	$R_t \pm \delta_{R_t}$ (nm)	$d \pm \delta_d$ (nm)	$R \pm \delta_R$ (nm)
2a	0.2	12 ± 3	8 ± 3	11 ± 3	80 ± 50
2b	1.0	22 ± 3	8 ± 3	20 ± 3	50 ± 20
2c/e	0.3	17 ± 3	10 ± 3	16 ± 3	110 ± 40
4b	5.3	54 ± 5	10 ± 3	50 ± 6	61 ± 13
5a	9.0	70 ± 5	20 ± 5	59 ± 7	53 ± 11
8a	0.5	20 ± 5	10 ± 3	19 ± 5	90 ± 50
8b	3.3	28 ± 3	10 ± 3	23 ± 4	21 ± 7
8c	7.7	41 ± 3	10 ± 3	33 ± 5	21 ± 5
8d	10.5	112 ± 10	10 ± 3	108 ± 10	140 ± 30

Table 1 – Representative geometrical parameters extracted or derived from single experimental height profiles. The lateral size (d) was computed from the height (h) and apparent lateral size (d_{app}) of the aggregate and the nominal tip radius (R_t) provided by the manufacturer. The radius of curvature of the aggregate (R) was also computed. Uncertainties of calculated parameters were attributed via error propagation.

Figure	$[h_{min}; h_{max}]$ (nm)	$[d_{app,\,min}; d_{app,\,max}]$ (nm)	$[d_{min}; d_{max}]$ (nm)
2a	[0.1; 0.5]	[10; 20]	[10; 19]
2b	[0.5; 1.9]	[15; 25]	[14; 22]
2c/e	[0.1; 0.5]	[15; 35]	[15; 34]
4b	[1; 9]	[30; 80]	[29; 75]
5a	[4; 12]	[40; 100]	[31; 90]
8a	[0.3; 2]	[19; 36]	[18; 34]
8b	[2; 6]	[20; 45]	[15; 39]
8c	[2; 11]	[30; 50]	[27; 40]
8d	[2; 16]	[50; 140]	[48; 135]

Table 2 – Range of geometrical parameters extracted from the AFM topography images reported in this work.

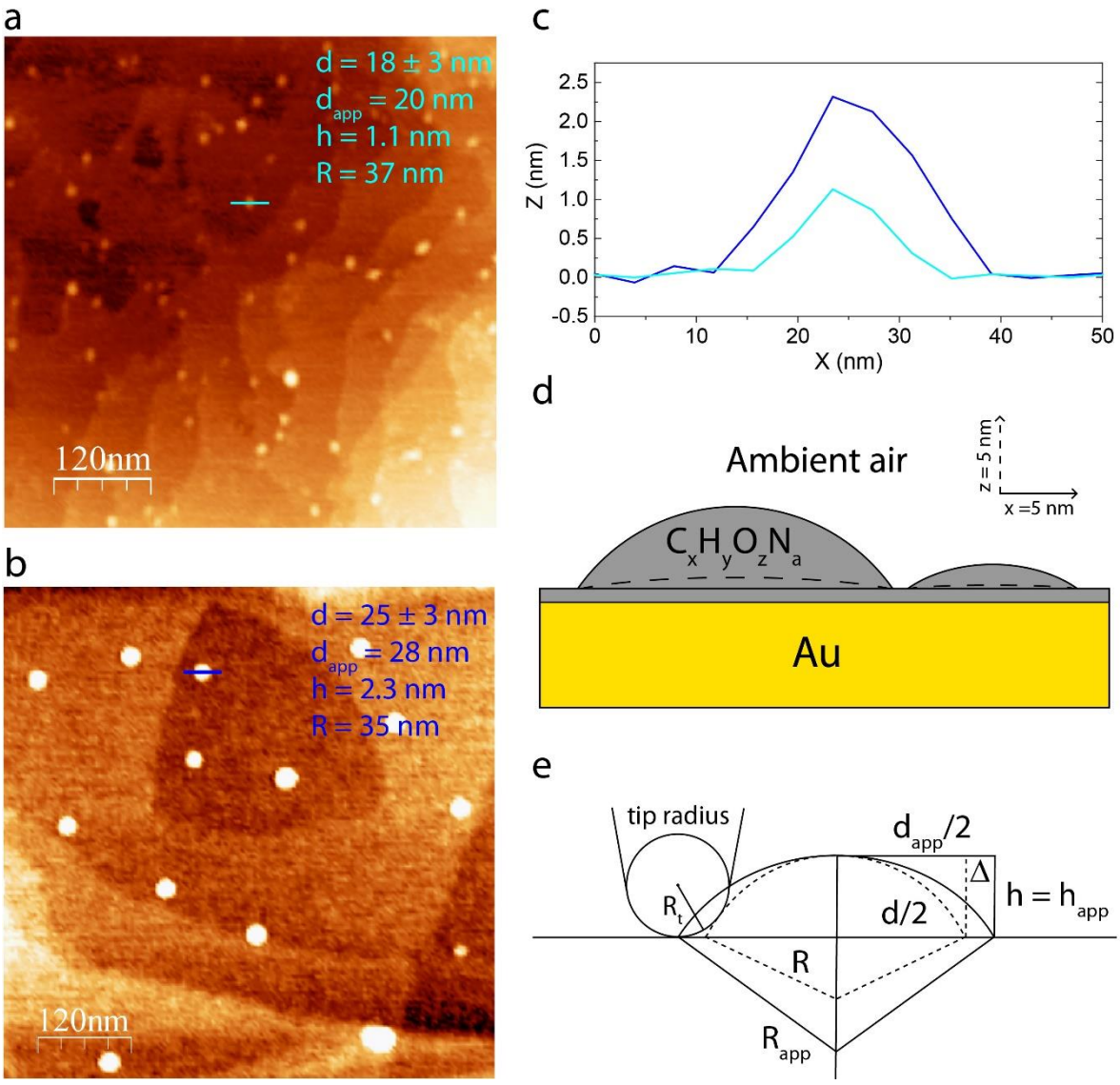

Figure 3: Ambient-AFM topography images of two contaminated Au(111) surfaces (a) recorded in non-contact mode, magnification from Figure 2b, and (b) recorded in intermittent contact mode, magnification from Figure S4c. Z-scale: (a, b) 2.9 nm. (c) Height profiles of the typical contaminant aggregates that are also indicated with cyan and blue horizontal lines in Figures 3a and 3b, respectively. (d) Schematic cartoon of an ideally-flat Au surface with a uniform contamination layer with contaminant aggregates on top at the interface with ambient air. (e) Geometrical model for the determination of the profile broadening due to the finite size of the tip. R, h and d are the curvature radius, the height and the lateral size of the aggregate, whereas R_{app}, h_{app} and d_{app} are the corresponding apparent parameters. R_t is the tip radius and $2\Delta = d_{app} - d$ is the effective profile broadening.

SEM imaging and EDX

To further characterize the AC layer on Au(111) surfaces, we performed SEM imaging in specific areas of the sample which were subsequently imaged by AFM. For this purpose, the samples were aged at ambient conditions until the contaminant aggregates were sufficiently large compared to the SEM lateral resolution. The surface topography of a contaminated Au sample was first obtained via SEM, by collecting the secondary electrons (Figure 4a), and then via AFM (Figure 4b). The aggregates monitored in the AFM image could be identified in the SEM image as darker spots, confirming the presence of aggregates with 30 nm < d < 80 nm. Grain boundaries were employed as topographical markers, enabling the imaging of the very same region by AFM and SEM, thereby providing a direct comparison between the two types of images (the method for searching the same sample region is illustrated in Section S5 and Figure S9). The EDX spectra was also recorded to obtain information about the chemical composition of the contaminant layer. Such measurements revealed a predominance of C, N and O elements onto the gold surface (see Figure S10).

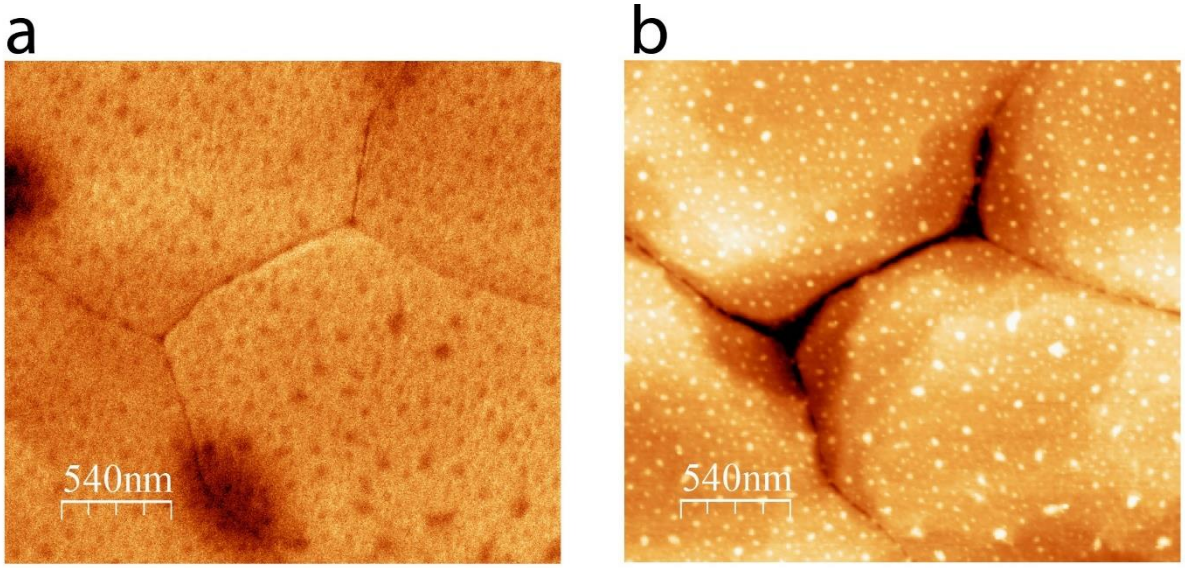

Figure 4: (a) SEM topography obtained from a Au(111) on mica sample after a long aging (> 3 months) with the secondary electrons detector, the acceleration voltage set at 20 kV, dwell time at 10 µs and chamber pressure ≈ 10^{-6} mbar. (b) Corresponding AFM topography collected at ambient conditions. Z-scale: 17.0 nm; n_s: 350 µm^{-2}.

KPFM measurements:

With the aim of clarifying the role of contaminant aggregates on the WF increase, we measured the local CPD via Kelvin probe force microscopy (KPFM). The presence of airborne contaminant aggregates induces a local change in the surface potential (SP) that is larger than the potential resolution (being below 10 mV)[67], as shown in Figure 5. For a metallic surface, the average CPD can be directly correlated to the SP or to the WF of the sample and a quite negligible correlation between the topography and the CPD images is expected for an oriented Au(111) sample. In particular, the CPD change associated with the height variation at a grain boundary (dark area in Figure 5a, around 20 nm dip) is comparable with the background noise, while 20-nm-thick aggregates exhibit CPD variations of $\Delta CPD \approx -25$ mV, as indicated by the profiles in Figure 5c.

However, the determination of the effective SP of a single nanometric aggregate is limited by the long-range electrostatic interactions ($\sim d^{-2}$) between the tip and the surface.[68] In the case of metallic samples, the electrostatic interaction only affects the surface and thus, solely the structures at the surface contribute to the measured potential.[45] In general, the lateral resolution of KPFM is on the order of a few tens of nanometers[67] and in the KPFM images reported here the achieved resolution is $\approx$ 50 nm. Thus, when the lateral size of the nanostructure is below 100 nm, the corresponding measured potential is underestimated, being the average of the effective value of the nanostructure and that of the surrounding substrate.[45] Such effect is visible in the upper-left side of Figure 5b, where aggregates are smaller and present in greater amount compared to the right side of the CPD image. In this region, the averaging effect dominates, thereby not allowing to measure significant potential variations. The smaller CPD of airborne contaminant aggregates compared to the rest of the surface suggests that electrons are withdrawn from the metal and accumulated at the metal/dielectric interface, as local surface charge densities can be detected via KPFM for charged defects that are at least 50 nm apart.[69] If the average CPD of the image at increasing aging times is considered instead, we found as well an increasing CPD, as visible in Figure S11. Hence, the contribution of the contaminant aggregates to the WF cannot be separated from the overall measured value which is determined by the ensemble of Au(111) and the AC layer.

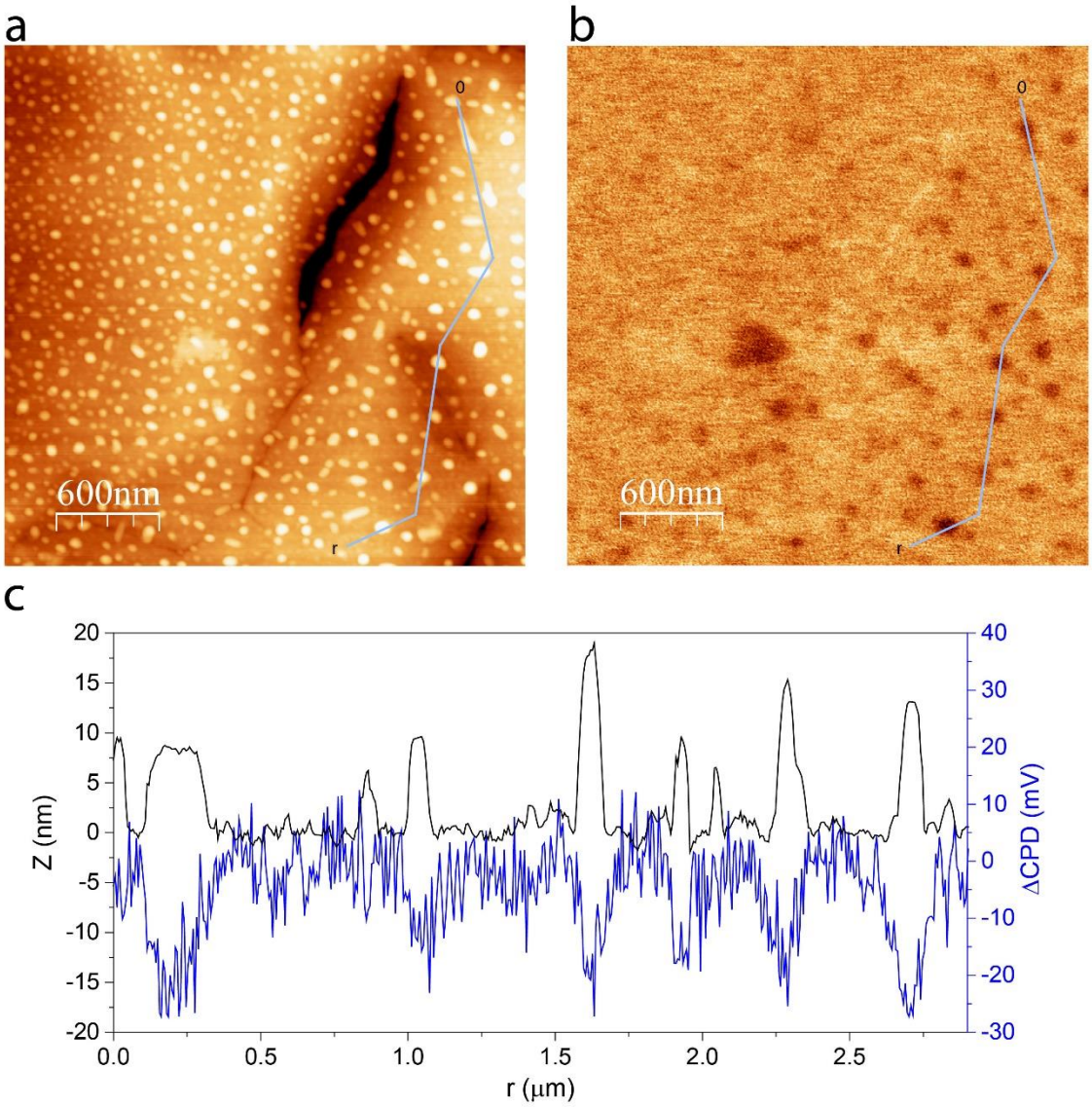

Figure 5: (a) Surface topography vs (b) CPD difference (3×3 μm^2) from a Au(111) on mica surface after a long aging (> 3 months) at laboratory conditions collected by amplitude-modulation KPFM in Bologna. The sample "as received" was aged at ambient conditions without prior cleaning. The Z-scale: (a) 34.2 nm, (b) is 43.6 mV, n_s: 200 μm^{-2}. (c) Height (black) and ΔCPD (blue) profiles along the path indicated with a grey line on the images above. The contribution of the substrate to the height profile was removed with a background subtraction to highlight the correspondence between height and CPD peaks.

Effect of storage conditions

The storage of Au(111) samples in closed environments, where the supply of contaminant aggregates inside the volume of the container is limited, revealed other peculiarities of contaminated Au(111) on mica surfaces. One obvious way to slow down the growth of the AC layer is by placing the samples inside a sealed container at ambient conditions. For this purpose, we compared the sample "as received" from the manufacturer (Figure 8a) and a sample from the same batch that was stored for 8 months in the storage container (Figure 8b). Note that the small container (≈ 50 cm^3) was occasionally opened for few minutes and then sealed again without gas any purging. These storage conditions represent the ordinary laboratory use of Au on mica samples. The size of contaminant aggregates found in the 8-month sample is larger while the number density (n_s) is still low (n_s = 40 μm^{-2}) compared to that recorded in an open-air system during the first days of contamination (Figure 2b). Aggregation processes are thus dominant over novel nucleation events of contaminant aggregates when gold is stored in a closed environment of reduced dimensions. This example highlights the slowing-down effects of the storage in a sealed container on the growth of aggregates. While ambient air is a potentially infinite reservoir of contaminants, the absorption of contaminant species and the growth of aggregates causes the partial pressure of these contaminants to drop in the storage container.

A further evidence of the growth and aggregation phenomena occurring during the storage in closed environments is that the n_s of aggregates tends to diminish while the aggregates increase in size. The AFM topography of a heavily contaminated sample before (Figure 8c) and after (Figure 8d) two days of storage inside a closed glass container is a clear example of the above-mentioned effect. We then measured the WF of TS Au(111) samples after repetitive cycles of 2-day storage in open (laboratory air) and closed environments (glass container). The change of the average WF and absolute PY slope is reported in Figure 9. The WF of samples in "closed" conditions was immediately measured after exposure (within 10 minutes). The WF consistently increased by $\approx$ 0.3 eV when the sample was exposed to laboratory air and decreased by $\approx$ 0.3 eV during storage in a closed container. The concomitant increase of the PY when samples were stored in closed conditions indicates that a significant fraction of the surface that was previously covered by aggregates got then uncovered. The growth of aggregates does not stop when the sample is enclosed in a sealed container because the aggregation keeps taking place while the nucleation is hindered. The surface mechanism explaining the observed trend of PY slope is the migration and merging of contaminant aggregates shown in Supplementary Video 1. This final example demonstrates the active contribution of contaminant aggregates to the change of the Au(111) WF.

In conclusion, the two phases of surface contamination of Au(111) have a strikingly different impact on the WF, driving the WF change in opposite directions. During the first phase, the rapid change of the WF is due to the adsorption of contaminants. Subsequently, the growth and aggregation of contaminant aggregates provides a mechanism for segregation of molecular contaminants at the gold/air interface which significantly affects the observed WF values. The long exposure of gold samples to ambient conditions leads to an increase of the WF with respect to the minimum observed in the KP and PYS curves. The interaction at the interface between the Au surface and the contaminant aggregates underlies the increment in the average WF that can thus be explained by considering the metal/dielectric (aggregates) system as a whole. When putting the sample in an open/closed environment a reversible change in WF was measured, revealing the dynamic reorganization of the contaminated gold surface mediated by the aggregates.

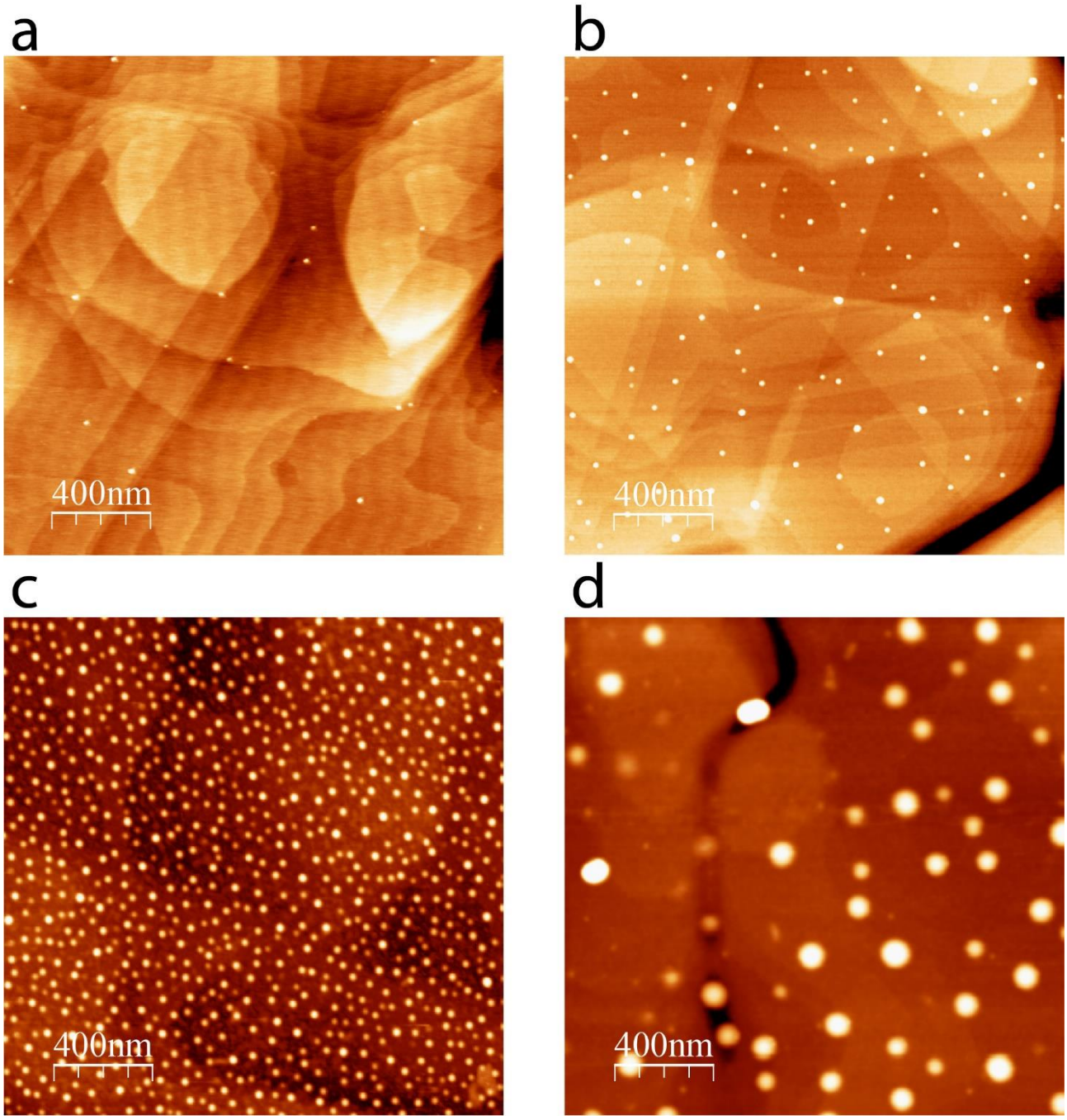

Figure 8: Ambient-AFM topography of contaminated Au(111) on mica (a) "as received" from the manufacturer and (b) after 8 months of storage in a closed and sealed container that was occasionally opened during laboratory activity. Effect of closing an AC contaminated Au(111) sample inside a sealed container for 2 days, (c) before and (d) after. AFM topography of Z-scale: (a) 2.5 nm, (b) 8.9 nm, (c) 10 nm, (d) 18 nm; n_s: (a) 15 μm^{-2}, (b) 40 μm^{-2}, (c) 300 μm^{-2}, (d) 40 μm^{-2}.

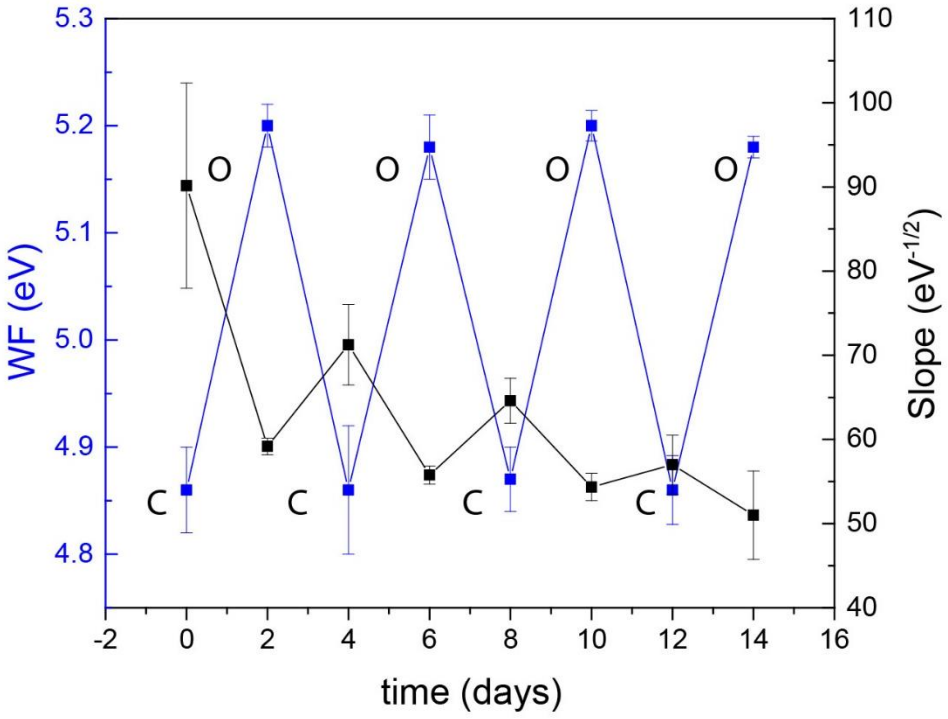

Figure 9: WF (black squares) vs PY slope (blue squares) changes of Au(111) on mica upon cycles of exposure to ambient conditions and closing in a glass container. O and C letters in the graph indicate the storage conditions (O = open laboratory air, C = closed in a glass container).

Methods (draft):

Preparation of Au(111) on mica samples in UHV:

Commercially available epitaxial Au(111) thin films grown on mica substrates manufactured by Phasis (Geneva, Switzerland) were transferred in a UHV chamber kept at a base pressure $p \approx 10^{-9}$ mbar. The samples were cleaned via repeated cycles of sputtering and annealing at 400°C and the surface composition was monitored via XPS until the absence of C 1s and O 1s signals was achieved. The absence of residual contaminant aggregates was further confirmed via *in-situ* STM imaging (see Figure S1a). The sputter-cleaning was performed with an Ar^+ ion gun set at an accelerating voltage of 1.5 kV and at a chamber pressure $p = 4.5 \times 10^{-6}$ mbar. After cleaning, the samples were transferred to ambient air and kept stored inside open containers at ambient conditions when not used for analysis.

Aging of Au(111) on mica samples:

Aging experiments in Strasbourg were done by using epitaxial Au(111) thin films grown on mica (Georg Albert PVD, Heidelberg, Germany). Au samples were used both "as received", hence with a pre-existing contamination layer, or after peeling off with bi-adhesive copper tape, thus exhibiting the "clean" side of the Au film. The Au films on the copper tape were then stuck on the backside of Si wafers to obtain a flat sample for AFM imaging and contact angle measurements. The contact angle of mica was below 10° and that of copper tape was above 115°.

Instrumentation:

AFM measurements were performed in Padova and in Strasbourg. In Padova, the AFM images were recorded at ambient conditions with an Agilent 5500 Scanning Probe Microscope equipped with an Agilent N9521A scanner. The vertical noise declared by the manufacturer (0.5 Å RMS) is in accordance with our experimental observations. The measurements were performed in non-contact mode with NanoWorld NCSTR probes (tip radius = 8 ± 3 nm, resonant frequency ≈ 160 kHz, k ≈ 7.4 $N \cdot m^{-1}$). In Strasbourg, the AFM images were recorded in intermittent contact mode at ambient conditions with a Bruker Multimode (Bruker Tespa-V2 probes, tip radius = 10 ± 3 nm, resonant frequency ≈ 320 kHz, k ≈ 32 $N \cdot m^{-1}$). Phase contrast and associated topography images were collected in intermittent contact mode at ambient conditions with a Bruker Dimension Icon AFM (Bruker Tespa-V2 probes) equipped with an optical microscope.

The Multimode AFM, equipped with an Extender Electronics module, was employed for KPFM experiments. Topography and CPD images were simultaneously collected at ambient conditions with Pt/Ir coated silicon probes (Bruker SCM-PIT, resonant frequency ≈ 75 kHz, k ≈ 2.8 $N \cdot m^{-1}$). The KPFM data presented in this work have been acquired in the amplitude modulation mode. The SPM

image processing has been done on WSxM software.[70] KP measurements were performed at ambient conditions on “as received” Au(111) on mica samples using a 2-mm-diameter gold tip amplifier (Ambient Kelvin Probe Package from KP Technology Ltd). The calibration of the probe was performed against a freshly cleaved highly-oriented pyrolytic graphite (HOPG) surface.[71] PY curves were recorded using a Riken Keiki spectrophotometer (Japan) model AC-2. The instrument was operated with an energy step of 0.05 eV and a UV spot intensity of 50 nW. SEM imaging was performed with a FEI Quanta FEG 250 operated at an accelerating voltage of 20 kV and at pressures below 10^{-6} mbar. The SEM images were collected with the detector for secondary electrons. Contact angle of sessile water drops on gold surfaces were measured with a Krüss DSA100 Drop Shape Analyser.

XPS spectra were recorded at room temperature at a base pressure of 10^{-9} mbar using a VG Scienta XM 650 X-ray source operated at 12 kV and 30 mA. The X-rays were monochromatized using a VG Scienta XM 780 monochromator optimized for Al Kα radiation (1486.7 eV). Photoelectrons were collected at normal incidence and analyzed with a Scienta SES 100 hemispherical electron analyzer operated at constant pass energy of 200 eV. The wide range spectra were collected with an energy step of 2 eV. Au $4f_{7/2}$ signal at 84.0 eV was used to calibrate the binding energy scale of the XPS spectra. Peak areas were calculated from Au 4f, C 1s and O 1s signals according to the Shirley method.[72] Relative peak area ratios expressed as atomic percentages were calculated from reference atomic sensitivity factors (ASF)[73] and accounting for the transmission properties of the analyzer. After cleaning the surface with sputtering and annealing cycles, the Au(111) on mica samples were transferred to the ambient environment and stored in an open container for a fixed amount of time until the XPS measurement. The samples were transferred again inside the UHV system through a pre-chamber, pumped down to 10^{-6} mbar within one hour, and then moved to the main chamber.

Conclusions:

The physical and chemical properties of gold surfaces are dynamic as they strongly depend on the surrounding environment. Alongside the well-known and documented surface reconstruction of the thermodynamically unstable Au(111) surface,[74,75] the surface topography, composition and work function are found to change upon aging the samples at ambient conditions. We shed light over the disregarded phenomena of the airborne contamination of gold by unraveling the dynamic nature of Au(111), which showed a surface reorganization of the AC overlayer and an efficient segregation of contaminant species into aggregates. Two separate contamination regimes were identified: a starting rapid phase, where contaminant species are readily adsorbed within minutes from exposure to ambient conditions and reorganize on the surface, and a slow phase, during which the contaminant aggregates migrate and grow via aggregation, and carbon species accumulate over time. Previously unexplained WF variations have been rationalized via a multiscale and multitechnique approach which revealed the presence and growth of contaminant aggregates on the Au(111) surface. While surface contamination is often overlooked because of its intrinsic variability, we demonstrated the universal nature of our studies on Au(111) by pointing out the common behavior of gold samples upon aging at ambient conditions.

Our findings are relevant for both experimental and theoretical purposes. Since clean gold exhibits unstable surface properties at ambient conditions, an aging time of few weeks is required in order to obtain a gold surface with stable properties, implying, for instance, that an equilibration period at ambient conditions must be included for KP or KPFM tip calibration. The generally wrong claim regarding the inert nature of gold accompanied by a stable WF holds true only after a careful preparation and storage of the reference sample. Moreover, we provided a simple picture for the geometrical modelling of contamination, useful for signal correction in X-ray techniques (e.g. XPS, EDX and XRR), and we first reported on the effect of the contamination dynamics on the Au WF, the comprehension of which is critical for applications where planar bare gold is employed, such as charge control via UV photoemission in space-based systems (LISA[76,77] and TianQin[78]). We also foresee important implications in devices and applications thereof based on Au electrodes, e.g. in biosensing (SPR), opto-electronics, etc. Finally, these results comprehensively explain the mechanism underlying the major variability of Au WF at ambient conditions, having a dramatic impact on our fundamental understanding of surface contamination.

Acknowledgments

The work in Strasbourg was financially supported by EC through the ERC project SUPRA2DMAT (GA-833707), the Marie Curie ITN project UHMob (GA-811284), the Labex projects CSC (ANR-10-LABX-0026 CSC) and NIE (ANR-11-LABX-0058 NIE) within the Investissement d'Avenir program ANR-10-IDEX-0002-02, and the International Center for Frontier Research in Chemistry (icFRC).

References

1. Smith, T. The hydrophilic nature of a clean gold surface. *J. Colloid Interface Sci.* **75**, 51–55 (1980).
2. Wagner, C. D. Studies of the charging of insulators in ESCA. *J. Electron Spectrosc. Relat. Phenom.* **18**, 345–349 (1980).
3. Barr, T. L. & Seal, S. Nature of the use of adventitious carbon as a binding energy standard. *J. Vac. Sci. Technol. A* **13**, 1239–1246 (1995).
4. Baker, M. A. Plasma cleaning and the removal of carbon from metal surfaces. *Thin Solid Films* **69**, 359–368 (1980).
5. Wan, A., Hwang, J., Amy, F. & Kahn, A. Impact of electrode contamination on the α-NPD/Au hole injection barrier. *Org. Electron.* **6**, 47–54 (2005).
6. Piao, H. & McIntyre, N. S. Adventitious carbon growth on aluminium and gold–aluminium alloy surfaces. *Surf. Interface Anal.* **33**, 591–594 (2002).
7. O'Kane, D. F. & Mittal, K. L. Plasma cleaning of metal surfaces. *J. Vac. Sci. Technol.* **11**, 567 (2000).
8. Seah, M. P. & Spencer, S. J. Ultrathin SiO2 on Si. I. Quantifying and removing carbonaceous contamination. *J. Vac. Sci. Technol. A* **21**, 345–352 (2003).
9. Sugimoto, F. & Okamura, S. Adsorption Behavior of Organic Contaminants on a Silicon Wafer Surface. *J. Electrochem. Soc.* **146**, 2725 (1999).
10. Strein, E. (Liz) & Allred, D. Eliminating carbon contamination on oxidized Si surfaces using a VUV excimer lamp. *Thin Solid Films* **517**, 1011–1015 (2008).
11. Azuma, Y. & Kurokawa, A. Influence of contamination layer on thickness evaluation by X-ray reflectometry. *X-Ray Spectrom.* **48**, 345–350 (2019).
12. Biswas, P. K., De, A., Dua, L. K. & Chkoda, L. Work function of sol–gel indium tin oxide (ITO) films on glass. *Appl. Surf. Sci.* **253**, 1953–1959 (2006).
13. Wang, W. *et al.* Dependence of aluminum-doped zinc oxide work function on surface cleaning method as studied by ultraviolet and X-ray photoelectron spectroscopies. *Appl. Surf. Sci.* **257**, 3884–3887 (2011).
14. Sugiyama, K., Ishii, H., Ouchi, Y. & Seki, K. Dependence of indium–tin–oxide work function on surface cleaning method as studied by ultraviolet and x-ray photoemission spectroscopies. *J. Appl. Phys.* **87**, 295–298 (1999).
15. Strohmeier, B. R. Improving the wettability of aluminum foil with oxygen plasma treatments. *J. Adhes. Sci. Technol.* **6**, 703–718 (1992).
16. Mantel, M. & Wightman, J. P. Influence of the surface chemistry on the wettability of stainless steel. *Surf. Interface Anal.* **21**, 595–605 (1994).
17. Schrader, M. E. Ultrahigh-vacuum techniques in the measurement of contact angles. II. Water on gold. *J. Phys. Chem.* **74**, 2313–2317 (1970).
18. Buchman, S., Quinn, T., Keiser, G. M., Gill, D. & Sumner, T. J. Charge measurement and control for the Gravity Probe B gyroscopes. *Rev. Sci. Instrum.* **66**, 120–129 (1995).
19. Saraf, S. *et al.* Ground testing and flight demonstration of charge management of insulated test masses using UV-LED electron photoemission. *Class. Quantum Gravity* **33**, 245004 (2016).
20. Armano, M. *et al.* Sub-Femto-g Free Fall for Space-Based Gravitational Wave Observatories: LISA Pathfinder Results. *Phys. Rev. Lett.* **116**, 231101 (2016).

21. Chai, L. & Klein, J. Large Area, Molecularly Smooth (0.2 nm rms) Gold Films for Surface Forces and Other Studies. *Langmuir* **23**, 7777–7783 (2007).
22. Basagni, A. *et al.* Molecules–Oligomers–Nanowires–Graphene Nanoribbons: A Bottom-Up Stepwise On-Surface Covalent Synthesis Preserving Long-Range Order. *J. Am. Chem. Soc.* **137**, 1802–1808 (2015).
23. Müllegger, S. & Winkler, A. The influence of carbon on the adsorption/desorption kinetics and monolayer formation of p-quaterphenyl on Au(111). *Surf. Sci.* **574**, 322–330 (2005).
24. Taylor, C. E., Garvey, S. D. & Pemberton, J. E. Carbon Contamination at Silver Surfaces: Surface Preparation Procedures Evaluated by Raman Spectroscopy and X-ray Photoelectron Spectroscopy. *Anal. Chem.* **68**, 2401–2408 (1996).
25. Hüfner, S., Cohen, R. L. & Wertheim, G. K. Argon Ion Sputtering of Metallic Surfaces for ESCA Studies. *Phys. Scr.* **5**, 91–92 (1972).
26. Taglauer, E. Surface cleaning using sputtering. *Appl. Phys. A* **51**, 238–251 (1990).
27. Chelvayohan, M. & Mee, C. H. B. Work function measurements on (110), (100) and (111) surfaces of silver. *J. Phys. C Solid State Phys.* **15**, 2305–2312 (1982).
28. Lecoeur, J., Bellier, J. P. & Koehler, C. Comparison of crystalographic anisotropy effects on potential of zero charge and electronic work function for gold {111}, {311}, {110} and {210} orientations. *Electrochimica Acta* **35**, 1383–1392 (1990).
29. Adamov, M., Perović, B. & Nenadović, T. Electrical and structural properties of thin gold films obtained by vacuum evaporation and sputtering. *Thin Solid Films* **24**, 89–100 (1974).
30. Stognij, A. I., Novitskii, N. N., Tushina, S. D. & Kalinnikov, S. V. Preparation of ultrathin gold films by oxygen-ion sputtering and their optical properties. *Tech. Phys.* **48**, 745–748 (2003).
31. Kang, J. & Rowntree, P. A. Gold Film Surface Preparation for Self-Assembled Monolayer Studies. *Langmuir* **23**, 509–516 (2007).
32. Zimmerling, T. & Batlogg, B. Improving charge injection in high-mobility rubrene crystals: From contact-limited to channel-dominated transistors. *J. Appl. Phys.* **115**, 164511 (2014).
33. Nogues, C. & Wanunu, M. A rapid approach to reproducible, atomically flat gold films on mica. *Surf. Sci.* **573**, L383–L389 (2004).
34. Tsai, H. *et al.* Instability of gold oxide Au2O3. *Surf. Sci.* **537**, L447–L450 (2003).
35. Fuchs, P. Low-pressure plasma cleaning of Au and PtIr noble metal surfaces. *Appl. Surf. Sci.* **256**, 1382–1390 (2009).
36. Tsai, M.-Y. & Lin, J.-C. Preconditioning Gold Substrates Influences Organothiol Self-assembled Monolayer (SAM) Formation. *J. Colloid Interface Sci.* **238**, 259–266 (2001).
37. King, D. E. Oxidation of gold by ultraviolet light and ozone at 25 °C. *J. Vac. Sci. Technol. A* **13**, 1247–1253 (1995).
38. Rentenberger, S., Vollmer, A., Zojer, E., Schennach, R. & Koch, N. UV/ozone treated Au for air-stable, low hole injection barrier electrodes in organic electronics. *J. Appl. Phys.* **100**, 053701 (2006).
39. Moon, D. W., Kurokawa, A., Ichimura, S., Lee, H. W. & Jeon, I. C. Ultraviolet-ozone jet cleaning process of organic surface contamination layers. *J. Vac. Sci. Technol. A* **17**, 150–154 (1999).
40. Yang, Z. *et al.* Analytical application of self assembled monolayers on gold electrodes: critical importance of surface pretreatment. *Biosens. Bioelectron.* **10**, 789–795 (1995).

41. Guo, L.-H., Facci, J. S., McLendon, G. & Mosher, R. Effect of Gold Topography and Surface Pretreatment on the Self-Assembly of Alkanethiol Monolayers. *Langmuir* **10**, 4588–4593 (1994).
42. Fischer, L. M. *et al.* Gold cleaning methods for electrochemical detection applications. *Microelectron. Eng.* **86**, 1282–1285 (2009).
43. Carvalhal, R. F., Sanches Freire, R. & Kubota, L. T. Polycrystalline Gold Electrodes: A Comparative Study of Pretreatment Procedures Used for Cleaning and Thiol Self-Assembly Monolayer Formation. *Electroanalysis* **17**, 1251–1259 (2005).
44. Martinez-Martin, D. *et al.* Atmospheric contaminants on graphitic surfaces. *Carbon* **61**, 33–39 (2013).
45. Liscio, A. *et al.* Local Surface Potential of π-Conjugated Nanostructures by Kelvin Probe Force Microscopy: Effect of the Sampling Depth. *Small* **7**, 634–639 (2011).
46. Baikie, I. D., Grain, A. C., Sutherland, J. & Law, J. Ambient pressure photoemission spectroscopy of metal surfaces. *Appl. Surf. Sci.* **323**, 45–53 (2014).
47. Kim, J. S. *et al.* Kelvin probe and ultraviolet photoemission measurements of indium tin oxide work function: a comparison. *Synth. Met.* **111–112**, 311–314 (2000).
48. Landoulsi, J. *et al.* Organic adlayer on inorganic materials: XPS analysis selectivity to cope with adventitious contamination. *Appl. Surf. Sci.* **383**, 71–83 (2016).
49. Swift, P. Adventitious carbon—the panacea for energy referencing? *Surf. Interface Anal.* **4**, 47–51 (1982).
50. Smith, G. C. Evaluation of a simple correction for the hydrocarbon contamination layer in quantitative surface analysis by XPS. *J. Electron Spectrosc. Relat. Phenom.* **148**, 21–28 (2005).
51. Gil, D. L. & Windover, D. Limitations of x-ray reflectometry in the presence of surface contamination. *J. Phys. Appl. Phys.* **45**, 235301 (2012).
52. Chauvet, C. *et al.* Carbon contamination of soft X-ray beamlines: dramatic anti-reflection coating effects observed in the 1 keV photon energy region. *J. Synchrotron Radiat.* **18**, 761–764 (2011).
53. Kahn, A. Fermi level, work function and vacuum level. *Mater. Horiz.* **3**, 7–10 (2016).
54. Uda, M. *et al.* Successive change in work function of Al exposed to air. *J. Electron Spectrosc. Relat. Phenom.* **88–91**, 767–771 (1998).
55. Sachtler, W. M. H., Dorgelo, G. J. H. & Holscher, A. A. The work function of gold. *Surf. Sci.* **5**, 221–229 (1966).
56. Krozer, A. & Rodahl, M. X-ray photoemission spectroscopy study of UV/ozone oxidation of Au under ultrahigh vacuum conditions. *J. Vac. Sci. Technol. A* **15**, 1704–1709 (1997).
57. Chesters, M. A. & Somorjai, G. A. The chemisorption of oxygen, water and selected hydrocarbons on the (111) and stepped gold surfaces. *Surf. Sci.* **52**, 21–28 (1975).
58. Wetterer, S. M., Lavrich, D. J., Cummings, T., Bernasek, S. L. & Scoles, G. Energetics and Kinetics of the Physisorption of Hydrocarbons on Au(111). *J. Phys. Chem. B* **102**, 9266–9275 (1998).
59. Ishii, H., Kinjo, H., Sato, T., Machida, S. & Nakayama, Y. Photoelectron Yield Spectroscopy for Organic Materials and Interfaces. in *Electronic Processes in Organic Electronics: Bridging Nanostructure, Electronic States and Device Properties* (eds. Ishii, H., Kudo, K., Nakayama, T. & Ueno, N.) 131–155 (Springer Japan, 2015). doi:10.1007/978-4-431-55206-2_8.
60. Kinoshita, S., Ohta, T. & Kuroda, H. Comments on the Energy Calibration in X-Ray Photoelectron Spectroscopy. *Bull. Chem. Soc. Jpn.* **49**, 1149–1150 (1976).

61. Friedel, B., Brenner, T. J. K., McNeill, C. R., Steiner, U. & Greenham, N. C. Influence of solution heating on the properties of PEDOT:PSS colloidal solutions and impact on the device performance of polymer solar cells. *Org. Electron.* **12**, 1736–1745 (2011).
62. Kagiyama, T., Saito, Y., Otobe, K. & Nakajima, S. Improvement of power performance in planar type AlGaAs/GaAs MESFET by substrate surface oxidation. *Appl. Surf. Sci.* **216**, 542–548 (2003).
63. Scott, W. W. & Bhushan, B. Use of phase imaging in atomic force microscopy for measurement of viscoelastic contrast in polymer nanocomposites and molecularly thick lubricant films. *Ultramicroscopy* **97**, 151–169 (2003).
64. Minj, A., Cavalcoli, D., Cavallini, A., Gamarra, P. & Poisson, M.-A. di F. Strain distribution and defect analysis in III-nitrides by dynamical AFM analysis. *Nanotechnology* **24**, 145701 (2013).
65. Borkent, B. M., de Beer, S., Mugele, F. & Lohse, D. On the Shape of Surface Nanobubbles. *Langmuir* **26**, 260–268 (2010).
66. Song, B., Walczyk, W. & Schönherr, H. Contact Angles of Surface Nanobubbles on Mixed Self-Assembled Monolayers with Systematically Varied Macroscopic Wettability by Atomic Force Microscopy. *Langmuir* **27**, 8223–8232 (2011).
67. Liscio, A., Palermo, V., Müllen, K. & Samorì, P. Tip−Sample Interactions in Kelvin Probe Force Microscopy: Quantitative Measurement of the Local Surface Potential. *J. Phys. Chem. C* **112**, 17368–17377 (2008).
68. Liscio, A., Palermo, V. & Samorì, P. Nanoscale Quantitative Measurement of the Potential of Charged Nanostructures by Electrostatic and Kelvin Probe Force Microscopy: Unraveling Electronic Processes in Complex Materials. *Acc. Chem. Res.* **43**, 541–550 (2010).
69. Rosenwaks, Y., Shikler, R., Glatzel, Th. & Sadewasser, S. Kelvin probe force microscopy of semiconductor surface defects. *Phys. Rev. B* **70**, 085320 (2004).
70. Horcas, I. *et al.* WSXM: A software for scanning probe microscopy and a tool for nanotechnology. *Rev. Sci. Instrum.* **78**, 013705 (2007).
71. Hansen, W. N. & Hansen, G. J. Standard reference surfaces for work function measurements in air. *Surf. Sci.* **481**, 172–184 (2001).
72. Shirley, D. A. High-Resolution X-Ray Photoemission Spectrum of the Valence Bands of Gold. *Phys. Rev. B* **5**, 4709–4714 (1972).
73. Chastain, J. Handbook of X-ray photoelectron spectroscopy. *Perkin-Elmer Corp.* **40**, 221 (1992).
74. Narasimhan, S. & Vanderbilt, D. Elastic stress domains and the herringbone reconstruction on Au(111). *Phys. Rev. Lett.* **69**, 1564–1567 (1992).
75. Needs, R. J. & Mansfield, M. Calculations of the surface stress tensor and surface energy of the (111) surfaces of iridium, platinum and gold. *J. Phys. Condens. Matter* **1**, 7555–7563 (1989).
76. Wass, P. J., Hollington, D., Sumner, T. J., Yang, F. & Pfeil, M. Effective decrease of photoelectric emission threshold from gold plated surfaces. *Rev. Sci. Instrum.* **90**, 064501 (2019).
77. Hechenblaikner, G. *et al.* Energy distribution and quantum yield for photoemission from air-contaminated gold surfaces under ultraviolet illumination close to the threshold. *J. Appl. Phys.* **111**, 124914 (2012).
78. Yang, F. *et al.* Investigation of charge management using UV LED device with a torsion pendulum for TianQin. *Class. Quantum Gravity* **37**, 115005 (2020).